Electronic Supplementary Material (ESI) for Journal of Materials Chemistry A.

Graphitic nanostructures in porous carbon framework significantly enhance the electrocatalytic oxygen evolution

Srinivas Gadipelli, [a,*] Zhuangnan Li,[a] Tingting Zhao,[a] Yuchen Yang,[a] Taner Yildirim[b] and Zhengxiao Guo[a]

[a]Department of Chemistry, University College London, 20 Gordon Street, London, WC1H 0AJ, UK

[b]NIST Center for Neutron Research, National Institute of Standards and Technology, Gaithersburg, Maryland, 20899, USA.

*Corresponding author: gsrinivasphys@gmail.com; s.gadipelli@ucl.ac.uk

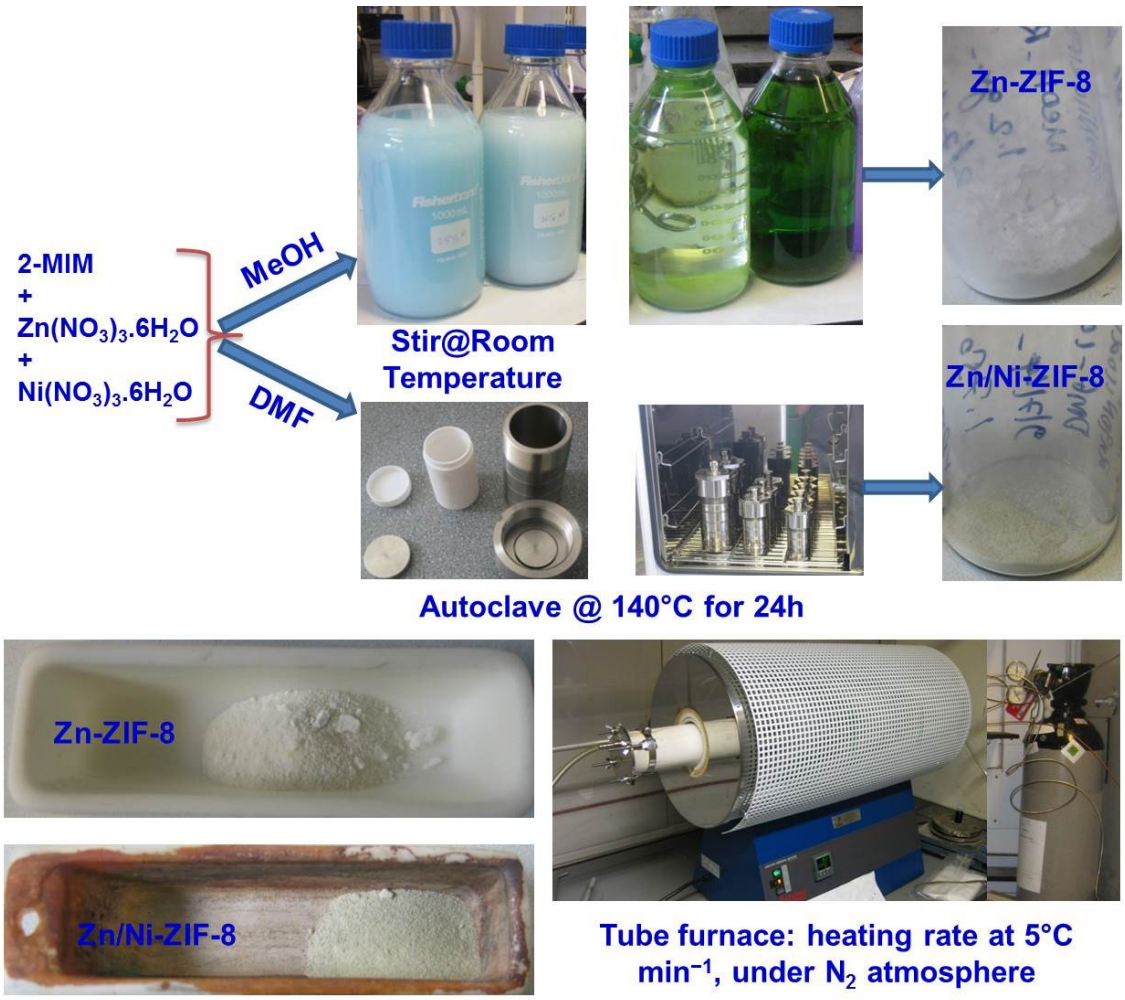

Figure S1. Synthesis of ZIF-8 and bimetallic Zn/Ni-ZIF-8 and their carbon nanostructure hybrids: The methanol solution stirring method at room temperature resulted only formation of Zn-ZIF-8.[5] The hydrothermal method yielded Zn/Ni-ZIF-8 from N,N-dimethylformamide solution of precursors.[44] The carbonization is carried out under inert gas, N_2 flow in a horizontal furnace.

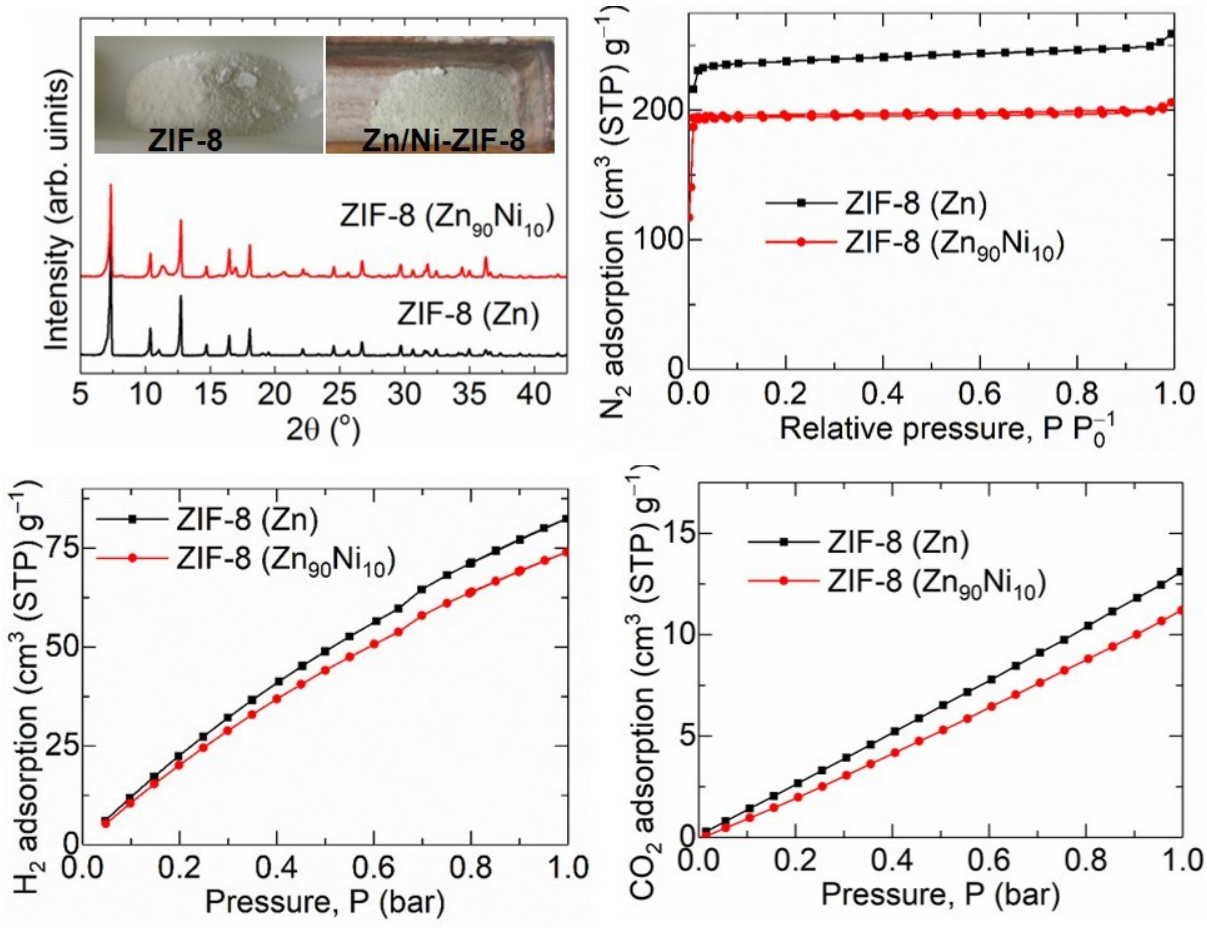

Figure S2. Structural characteristics of the Zn-ZIF-8 and Zn/Ni-ZIF-8 samples: PXRD patterns and photographs of the powder samples as inset (top-left), N_2 adsorption-desorption isotherms at 77 K estimates the BET surface area of 1000 $m^2\ g^{-1}$ for Zn-ZIF-8 and 840 $m^2\ g^{-1}$ for Zn/Ni-ZIF-8 (top-right), H_2 uptake isotherms at 77 K (bottom-left) and CO_2 uptake isotherms at 298 K (bottom- right).

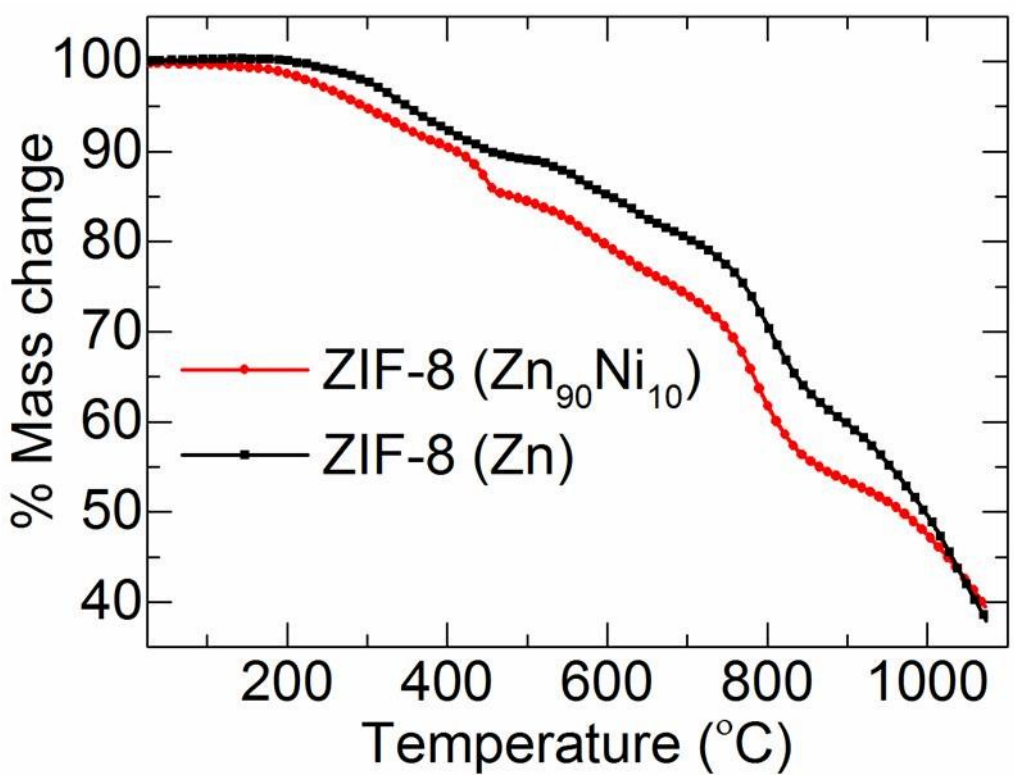

Figure S3. TGA curves of Zn-ZIF-8 and Zn/Ni-ZIF-8, measured under inert gas atmosphere with a heating rate of 5 °C min^{-1}, and up to 1080 °C.

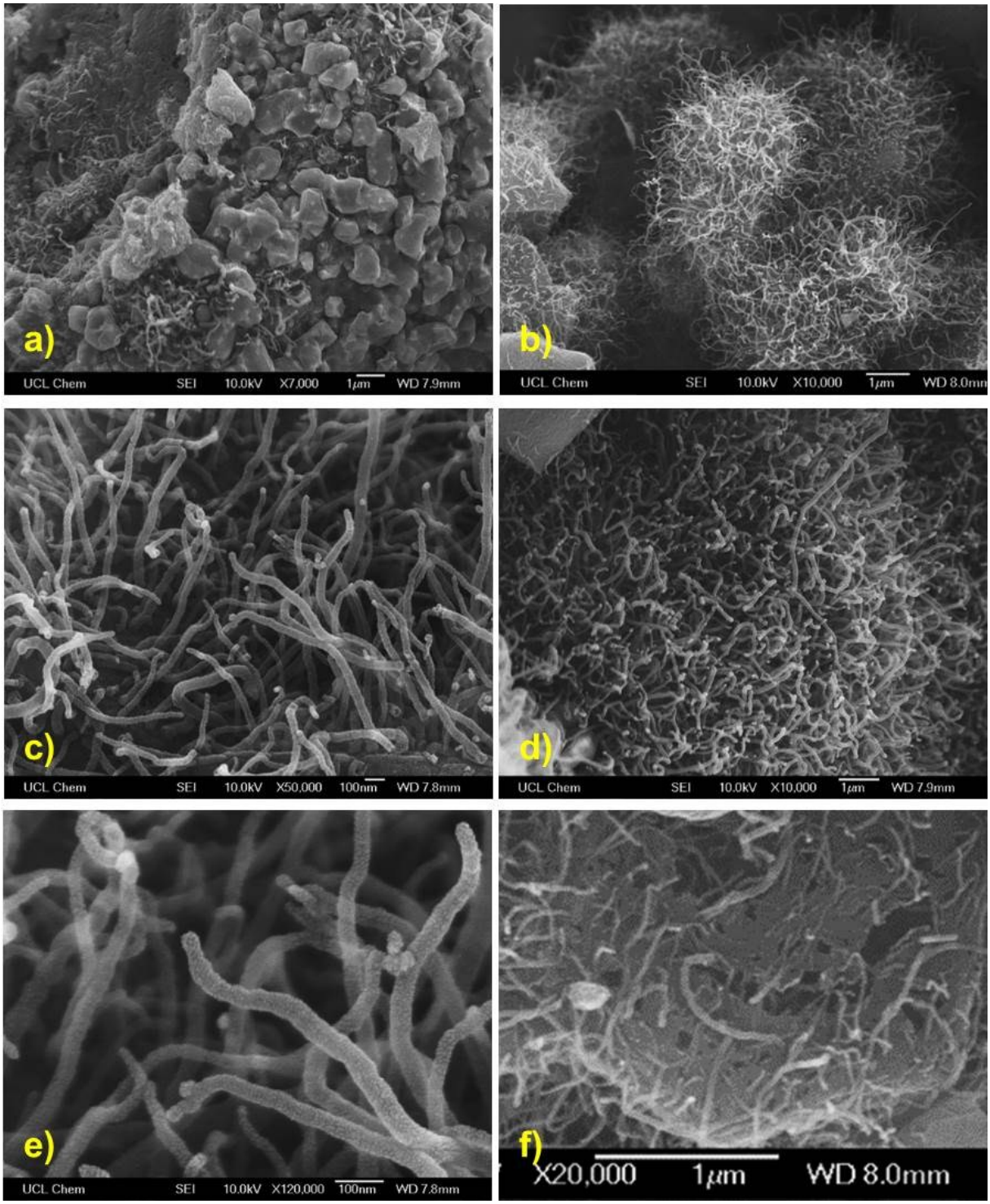

Figure S4. SEM micrographs of ZNDC1100 sample. A melting behaviour and onset growth of nanographites@porous carbon structure is seen in the sample heated to the target temperature 1100 °C and cooled down immediately (a). Surface gold coated nanoparticles are seen in the images taken at high magnifications (c & e).

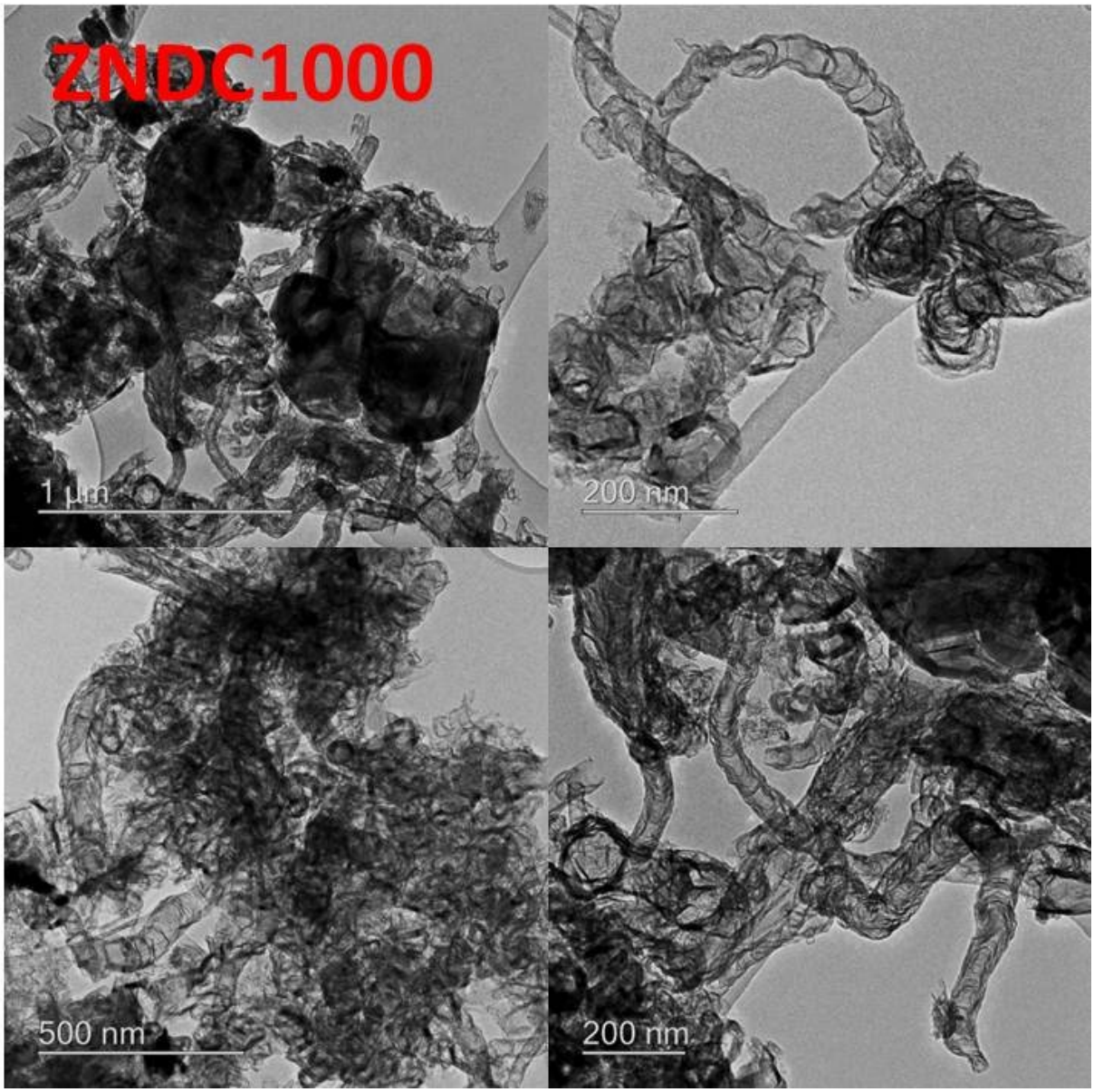

Figure S5. TEM micrographs of ZNDC1000 sample, showing a coexistence & growth of nanographitic structures in the amorphous type porous carbon.

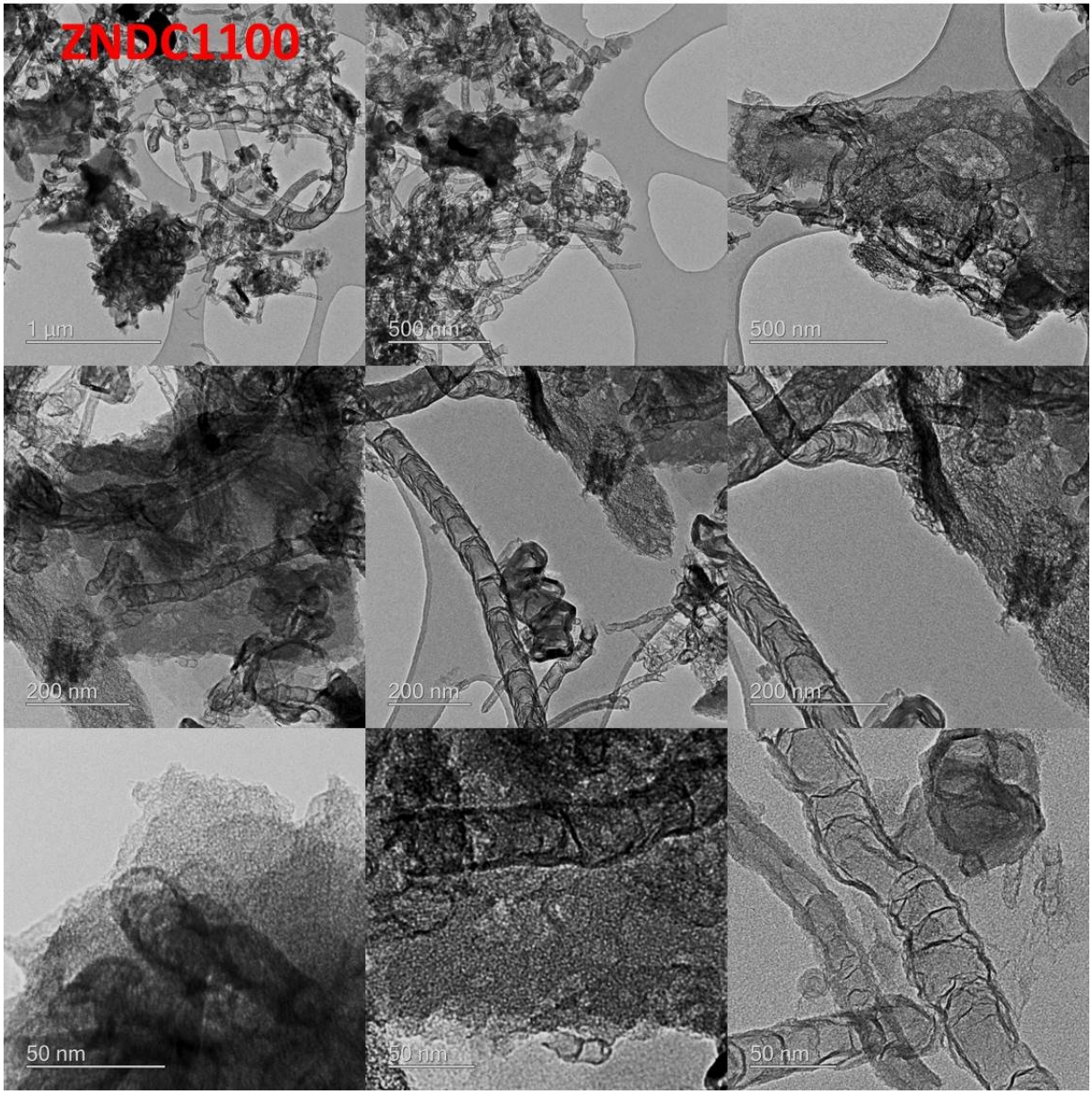

Figure S6. TEM micrographs of ZNDC1100 sample, showing a coexistence & growth of nanographitic structures in the amorphous type porous carbon.

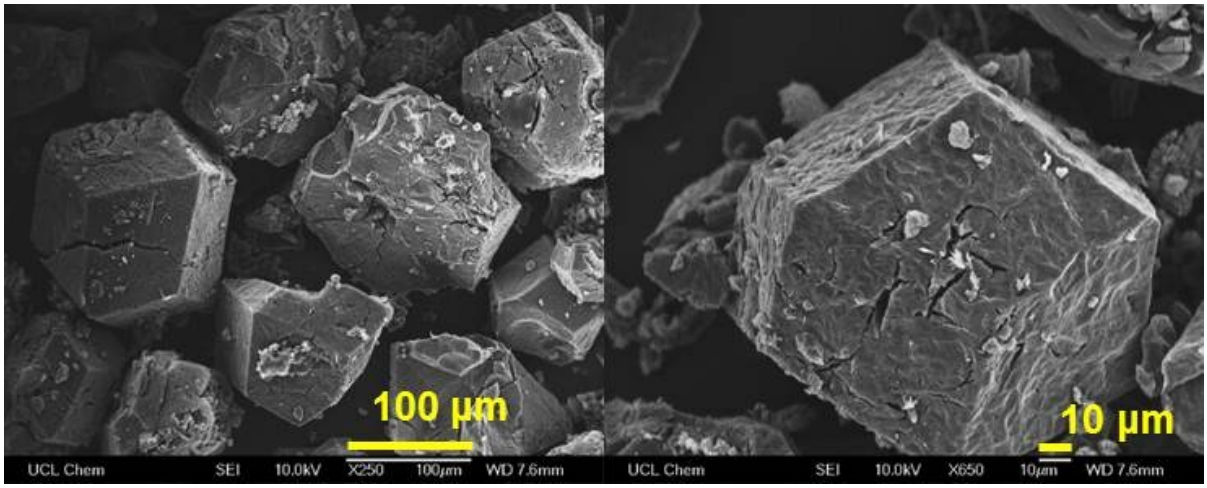

Figure S7. SEM micrographs of ZDC1000 derived from Zn-ZIF-8, shows only micro-cracks and surface shrinkage due to the evaporation of zinc metal together with the partial decomposition of the ligand.

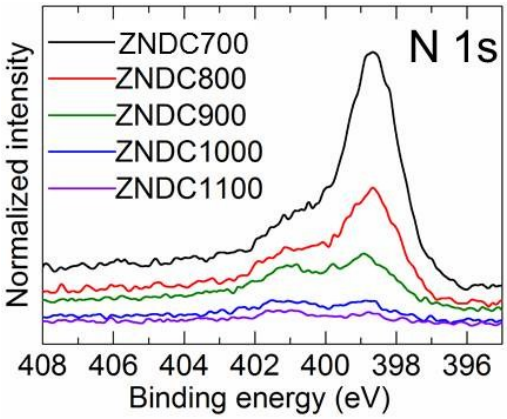

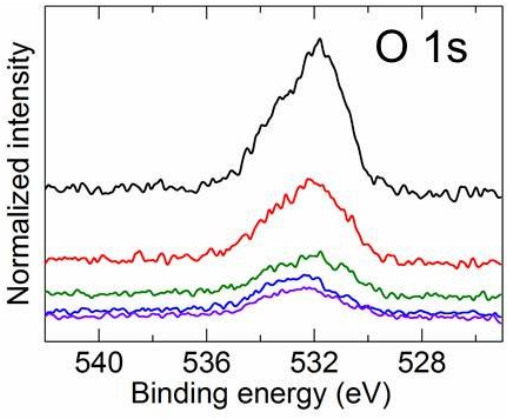

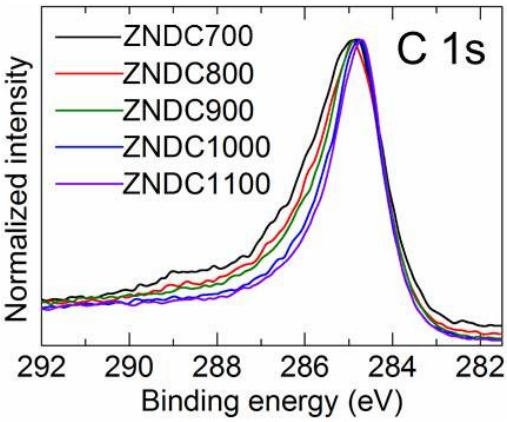

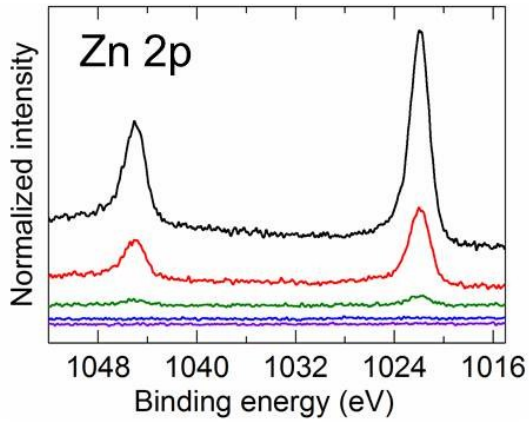

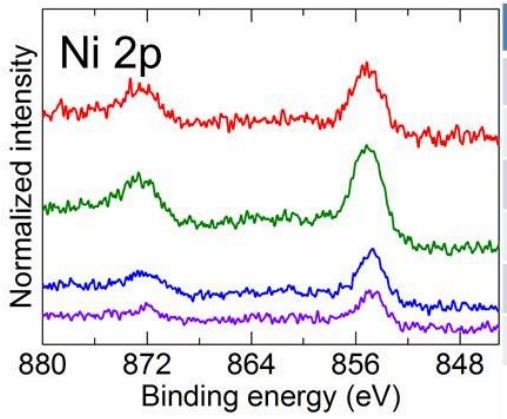

Sample	C	N	O	Zn	Ni
ZNDC700	73.60	15.60	8.10	2.70	
ZNDC800	82.00	10.00	6.20	1.40	0.40
ZNDC900	89.70	5.80	4.00	0.10	0.50
ZNDC1000	93.60	2.70	3.30	-	0.45
ZNDC1100	95.20	1.80	2.65	-	0.35
ZDC1000	89.70	3.00	7.30	-	-

Figure S8. XPS spectra of N 1s (top-left), O 1s (top-right), C 1s (middle-left), Zn 2p (middle-right), and Ni 2p (bottom-left). Table shows the elemental composition in atom%. All the intensities showed are normalized to C 1s peak intensity. Same colour labels apply for all the plots. Framework and ligand decomposition can be understood from the N 1s and O 1s spectra. Oxygen is detected in the structure due to the atmosphere adsorbed moisture on the defective sites. Therefore, ZNDC700 sample shows highest oxygen content on high concentrated defect sites at C, N and Zn, generated by framework decomposition. Increase in the carbonization temperature leads to the transition from pyrrole N- type in the ZIF-8 to the pyridine N- and graphitic N-type. Increased carbonization temperature leads to the graphitization by loss of nitrogen. Complete evaporation of Zn metal happens at >900 °C. The reduced Ni content in the ZNDC1000 and ZNDC1100 compared to the ZNDC900 is the indication of graphitization at Ni centres leading to the shielding effect.

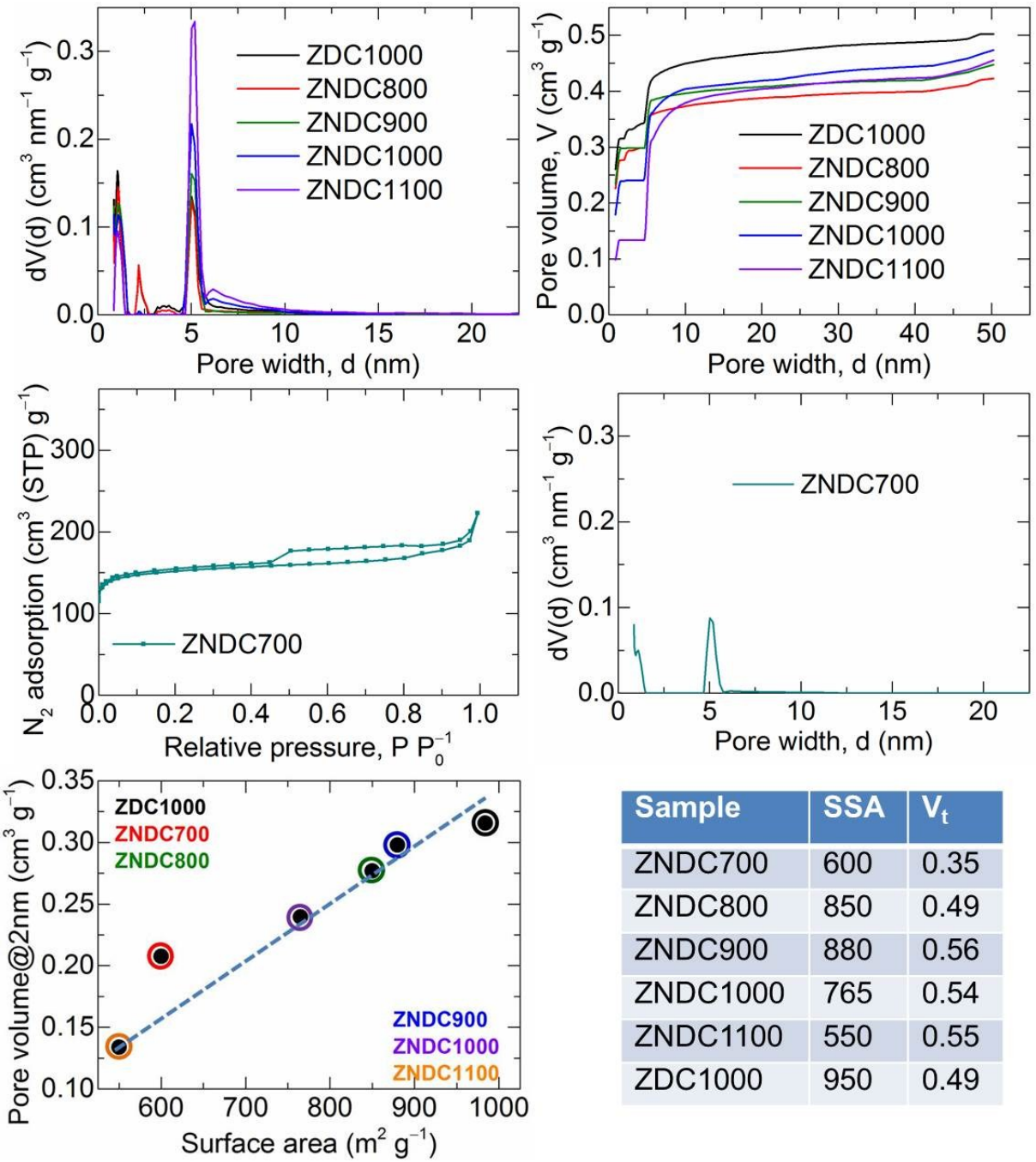

Sample	SSA	V_t
ZNDC700	600	0.35
ZNDC800	850	0.49
ZNDC900	880	0.56
ZNDC1000	765	0.54
ZNDC1100	550	0.55
ZDC1000	950	0.49

Figure S9. Porosity characteristics of the ZNDCs: Pore size distribution (top-left), cumulative pore volume (top-right) curves. Middle panel shows the N_2 adsorption-desorption isotherm and its QSDFT derived pore-size distribution for the ZNDC700 sample. Bottom-left plot shows the relation between QSDFT model derived total micropore volume at 2 nm and BET specific surface area (SSA) of the ZNDC and ZDC samples. Due to the framework decomposition, the ZNDC700 sample exhibits high microporosity. Table lists the BET SSA and total pore volume (V_t) of the samples.

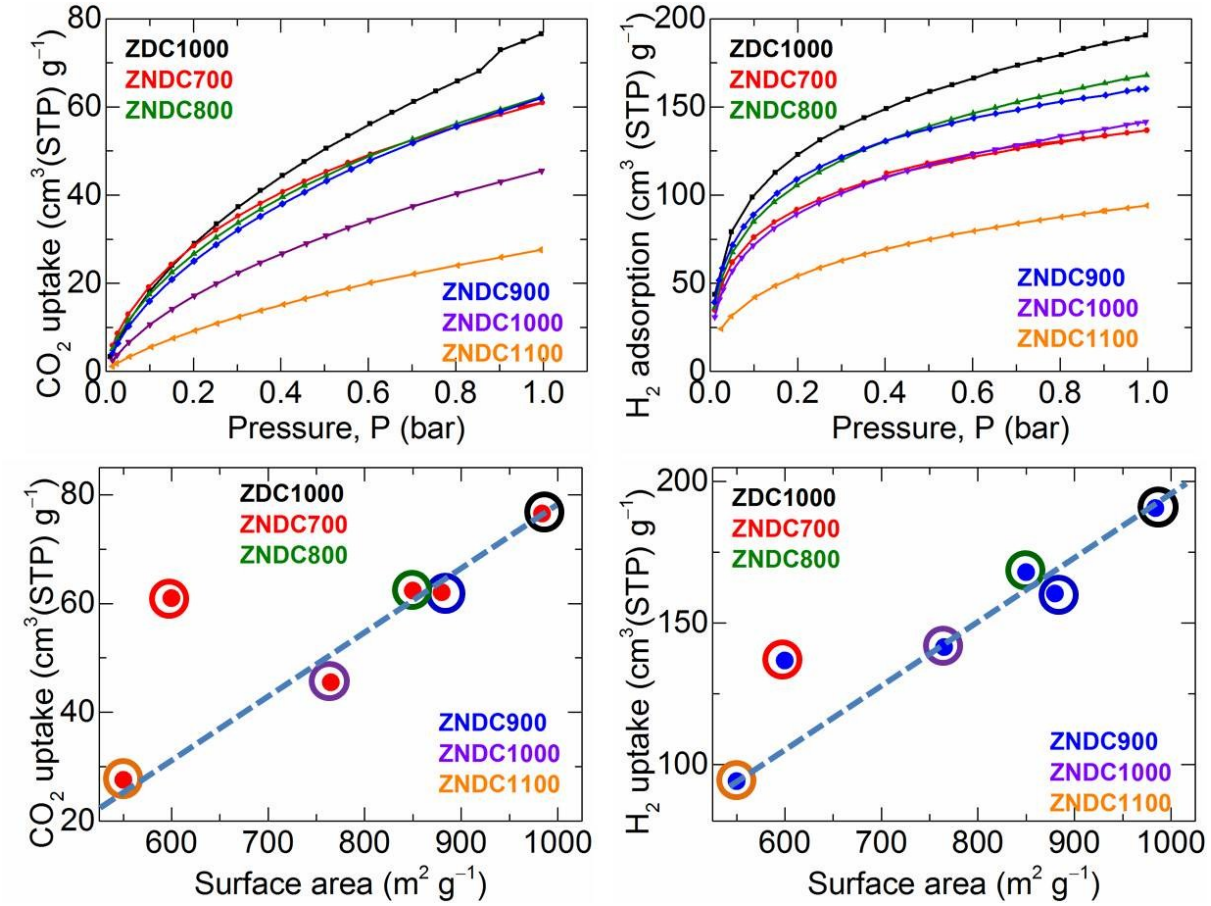

Figure S10. Structure and porosity induced gas uptake behaviour of ZNDCs: CO_2 uptake at 298 K (top-left) and H_2 uptake at 77 K (top-right) isotherms. Bottom two plots show the CO_2 and H_2 uptake at 1 bar against the BET surface area of the samples. High gas uptake in the ZNDC700 sample is directly attributed to the structure defects of active C, N and Zn cites and microporosity due to the framework decomposition.

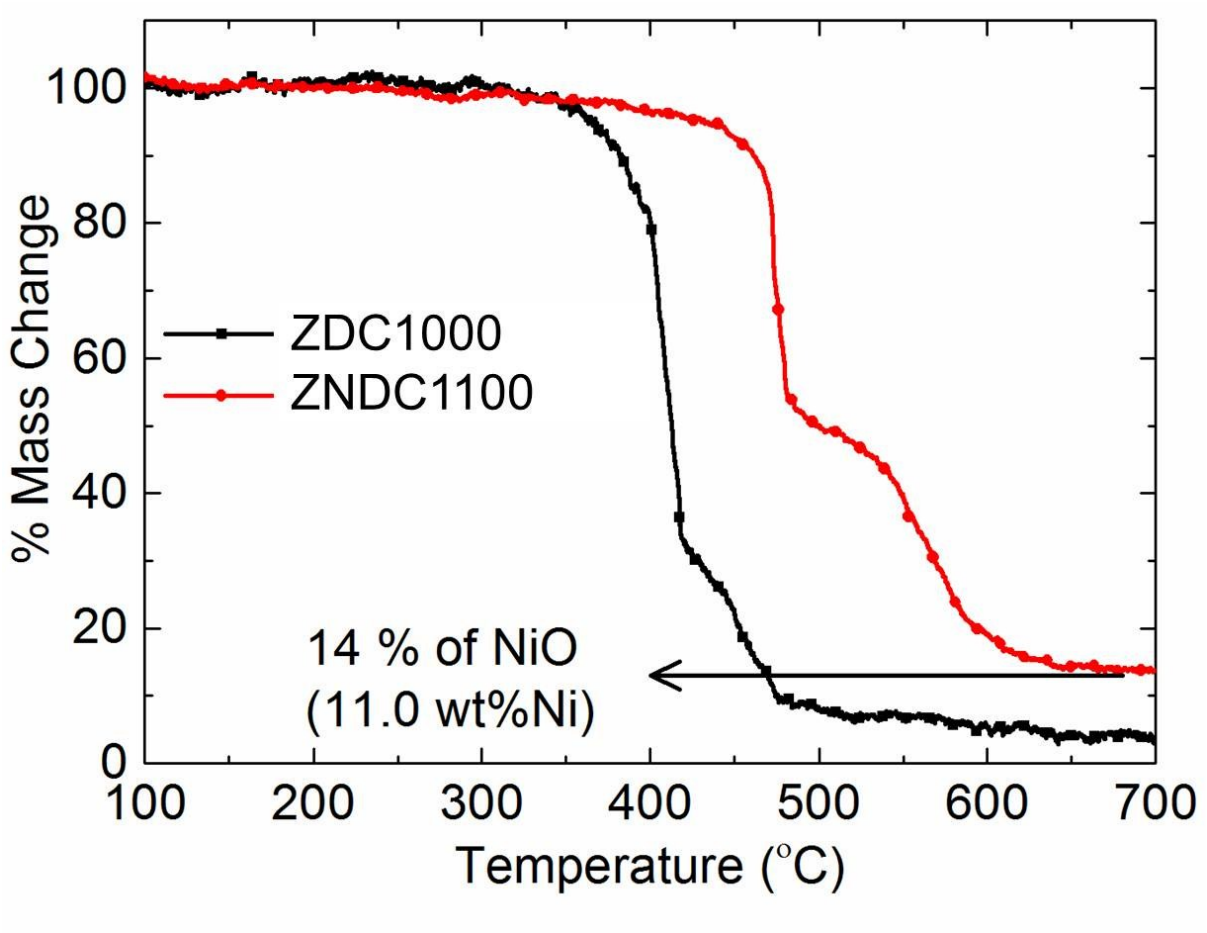

Figure S11. TGA curves of ZDC1000 and ZNDC1100 samples, measured under oxygen atmosphere with a heating rate of 5 °C per minute. See that different thermal stability of the samples is directly attributed to the amorphous and graphitized carbons. The two-step mass-loss in the ZNDC1100 sample indicates that porous carbon and nanographites in about 1:1 weight ratio. Complete burning of the carbon estimates about 11 mass% of nickel in the structure, calculated assuming Ni is in NiO state under high temperature and oxygen atmospheric conditions.

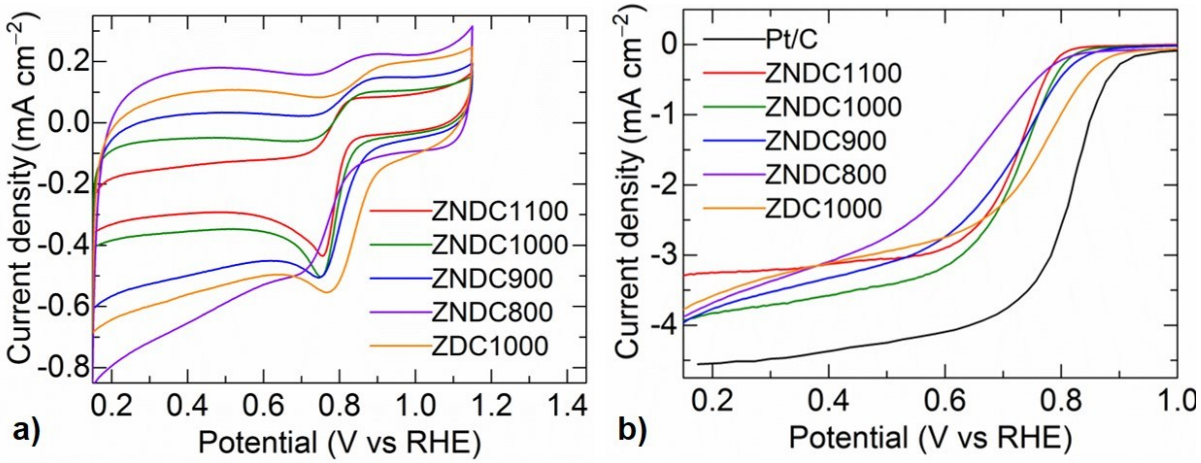

Sample	V_{ORR}	V_{OER}	$V_{Bifunct}$
ZNDC1100	0.561	1.667	1.106
ZNDC1000	0.630	1.735	1.105
ZNDC900	0.543	1.839	1.296
ZNDC800	0.424	2.000	1.576
ZDC1000	0.469	1.898	1.429

d)

Figure S12. CV curves for ORR (a) and polarization curves for ORR (b) and HER (c) of the ZNDC samples, measured under 0.1 M KOH electrolyte at a scan rate of 10 mV s^{-1}. ORR activity can be seen at development of more promising cathodic current peak at about 0.75 V (a). The enhanced ORR and HER activity can be understood either from increased current density at more positive potential, and also with a more positive on-set reaction potential. It was found that nickel nanocentres and its induced severe graphitization with a considerable loss of nitrogen functionality to reduce the heterogeneous surface and positive cores for effective oxygen adsorption in the structures eventually leads to unfavourable ORR activity (see reference 5 in the main text). The bifunctional activity of the samples for ORR and OER is summarized in table (d). Note that the potential is estimated from the difference between the OER (at 10 mA cm^{-2}) and ORR (at −3 mA cm^{-2}), and lower the difference better the bifunctional activity. Accordingly, ZNDC1100 and ZNDC1000 samples show better bifunctional activity compared to the ZDC1000, in its amorphous state. ZDC1000 sample require additional potential of about 320 mV to that of ZNDC1000 sample.

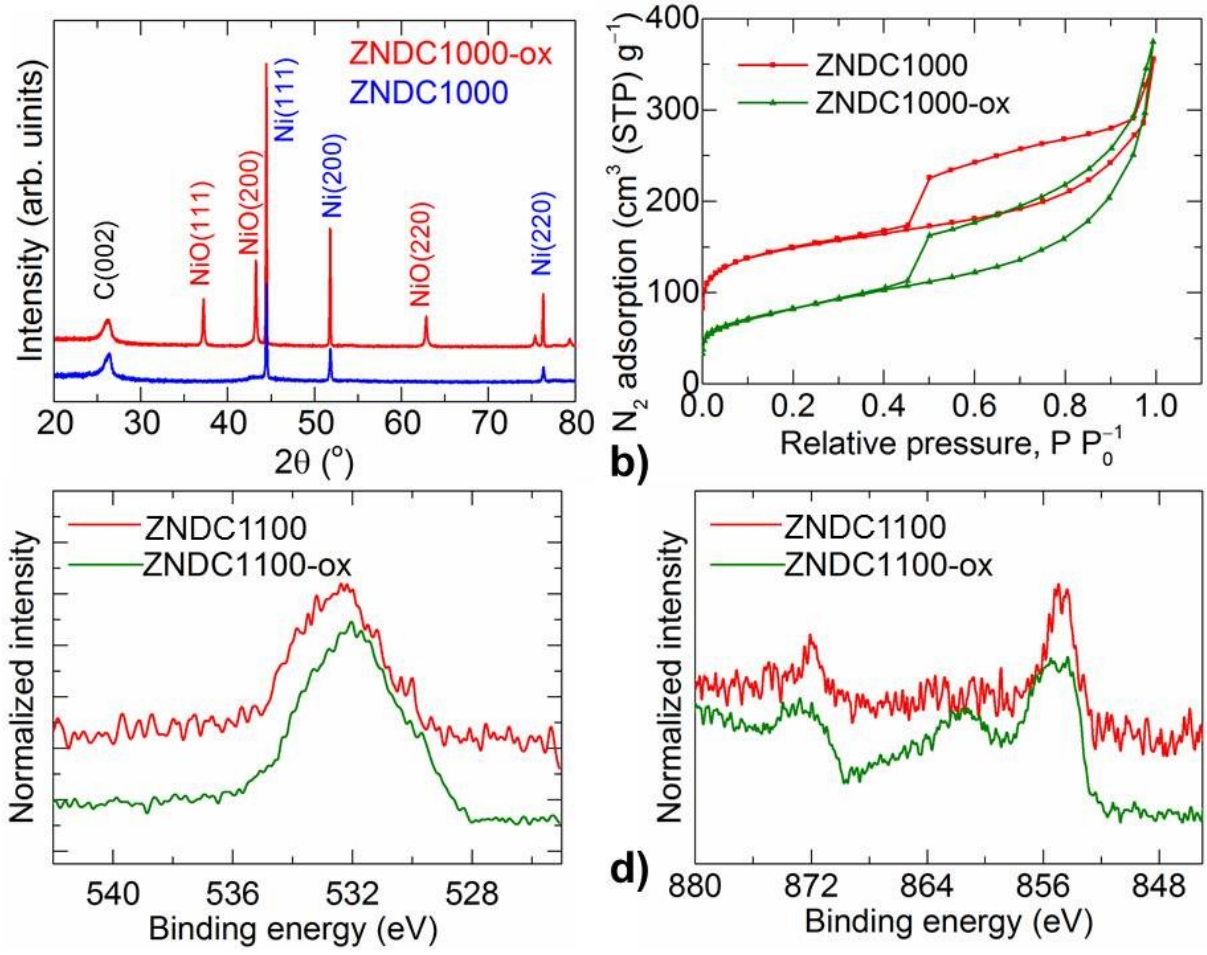

Figure S13. Structural characteristics of ZNDC1100-ox, sample obtained by controlled oxidation of ZNDC1100 sample. PXRD patterns show the partial surface oxidation of nickel to yield NiO@ Ni@C (a), N_2 adsorption-desorption isotherms of ZNDC1100 and ZNDC1100-ox samples reveal that reduced porosity in the oxidized samples, directly attributed to the partial burning of the porous carbon (b), XPS O 1s (c) and Ni 2p (d) spectra shows the formation of surface NiO@Ni in the ZNDC1100-ox sample.

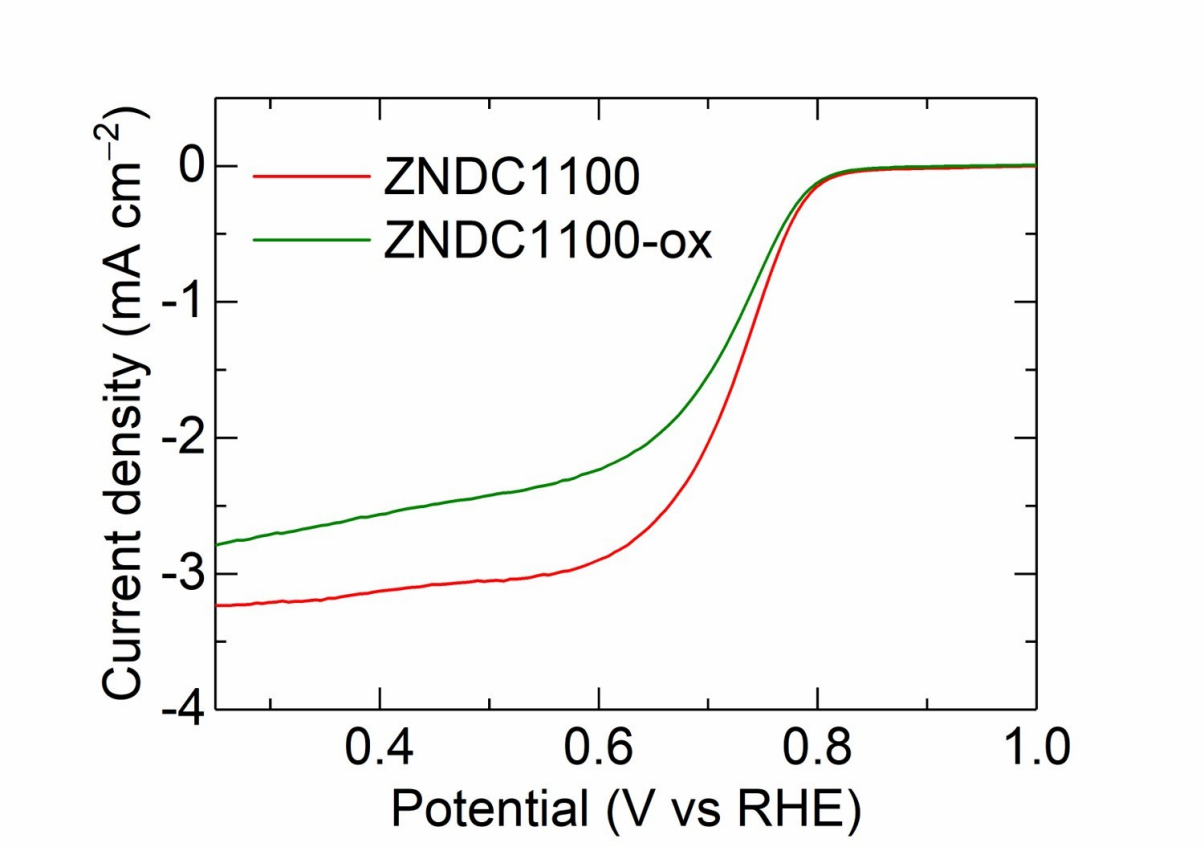

Figure S14. ORR polarization curves at 1600 rpm in a 0.1 M KOH electrolyte for the ZNDC1100 and ZNDC1100-ox samples, showing a reduced activity of the ZNDC1100-ox.

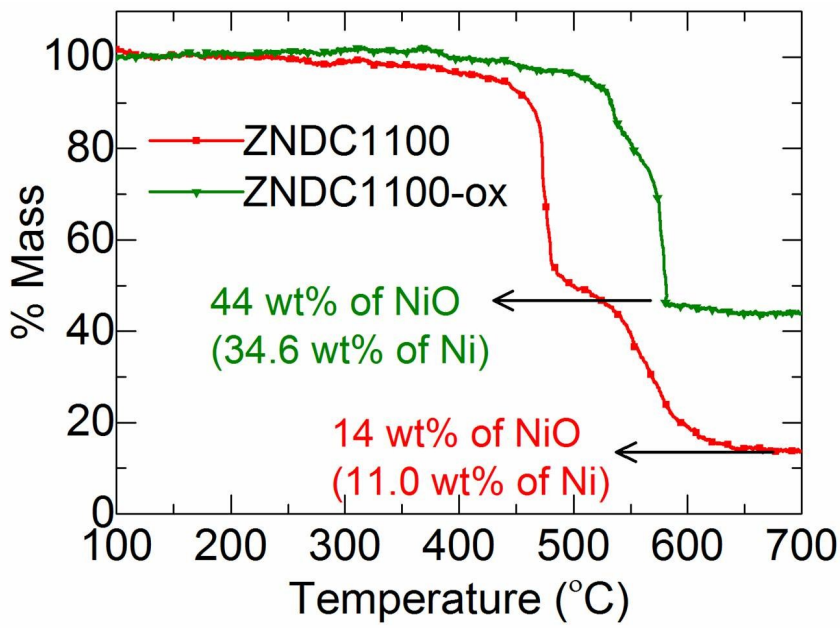

Figure S15. TG curves of ZNDC1100 and ZNDC1100-ox samples, measured under oxygen atmosphere with a heating rate of 5 °C per minute. See that different thermal stability of the samples is directly attributed to the amorphous and graphitized carbons. ZNDC1100-ox sample exhibits predominantly graphitized carbon. Complete burning of the carbon estimates about 35 mass% of Ni content in the ZNDC1100-ox sample, which is a three times higher than ~11 mass% Ni in the ZNDC1100 sample.

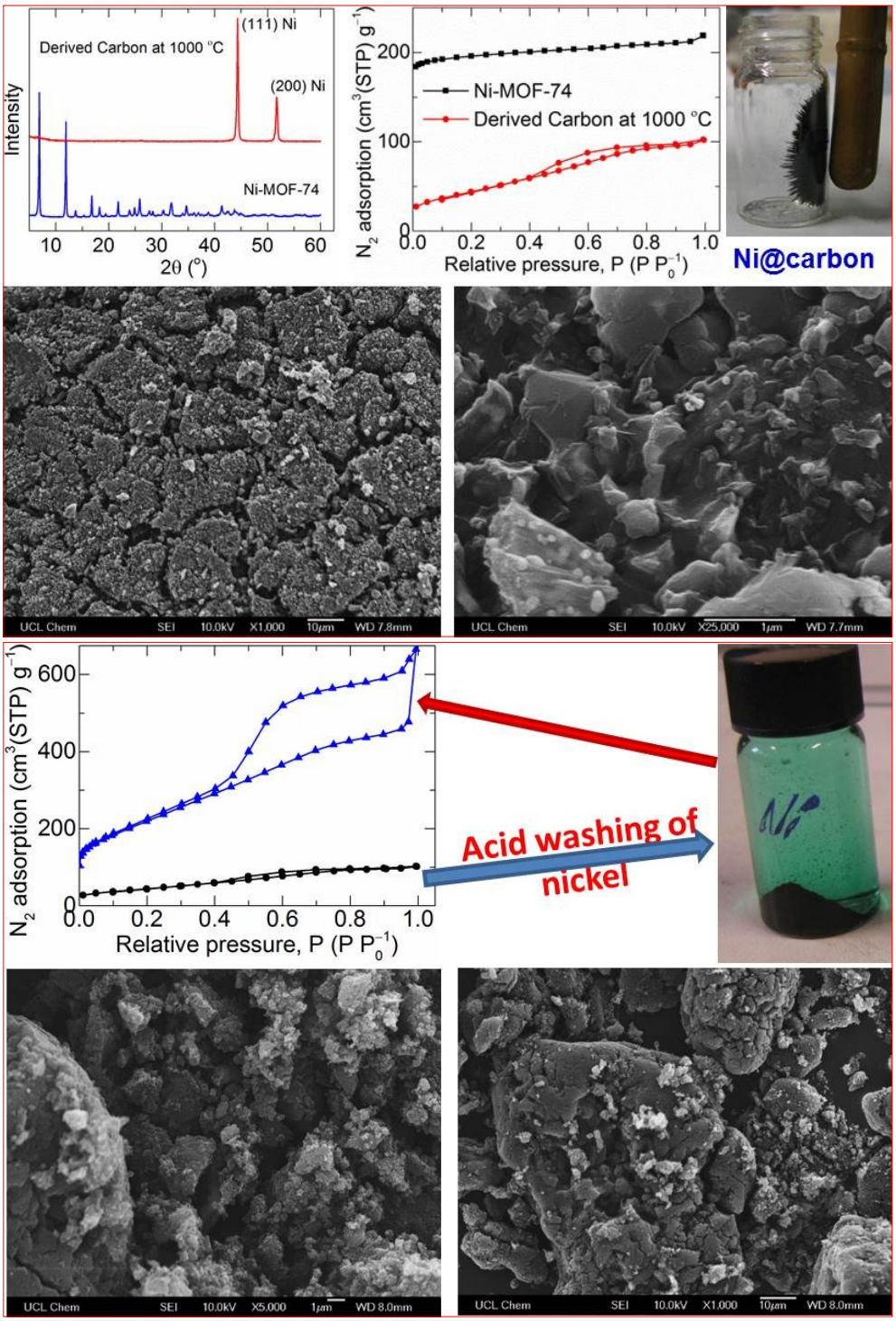

Figure S16.Characteristics of Ni-MOF-74 and derived carbons – as-synthesized and after acid etching of nickel. Top panel shows the PXRD patterns and N_2 adsorption-desorption isotherms (at 77 K) of the Ni-MOF-74 and MDC1000, and the magnetic behaviour and SEM micrographs of MDC1000. Bottom panel shows comparative N_2 adsorption-desorption isotherms of MDC1000 sample before and after acid washing, see the Ni^{2+} ions during the nickel etching under acid, and SEM micrographs of the MDC1000-aw. The samples exhibit BET SSA and total pore volume of (800, 150 & 710) $m^2\ g^{-1}$and (0.34, 0.16 & 1.03) $cm^3\ g^{-1}$, respectively for Ni-MOF-74, MDC1000 & MDC1000-aw.

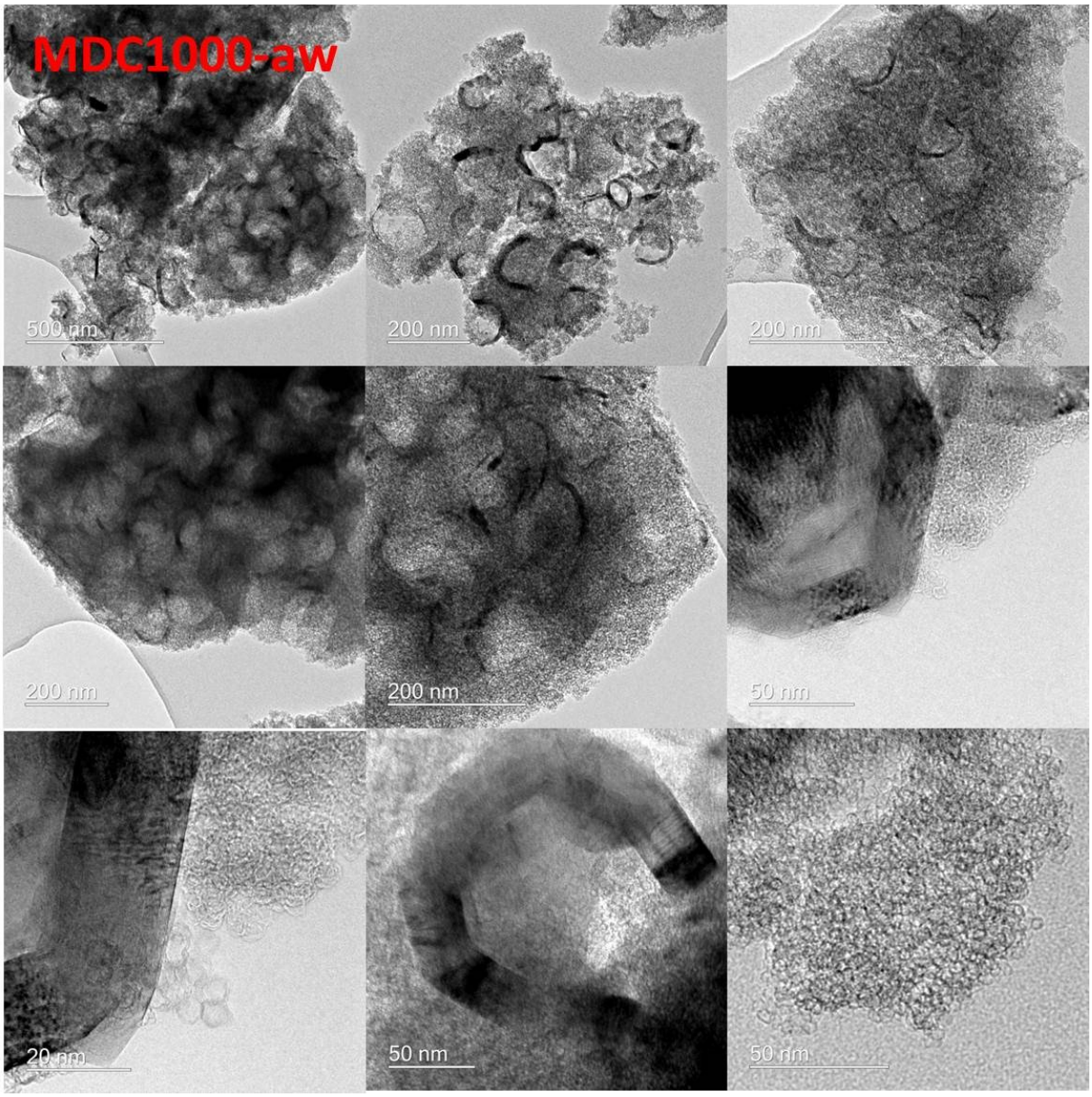

Figure S17. TEM micrographs of MDC1000-aw, showing predominant porous carbon with the regions of graphitic shells formed around nickel clusters (etched by HCl washing).

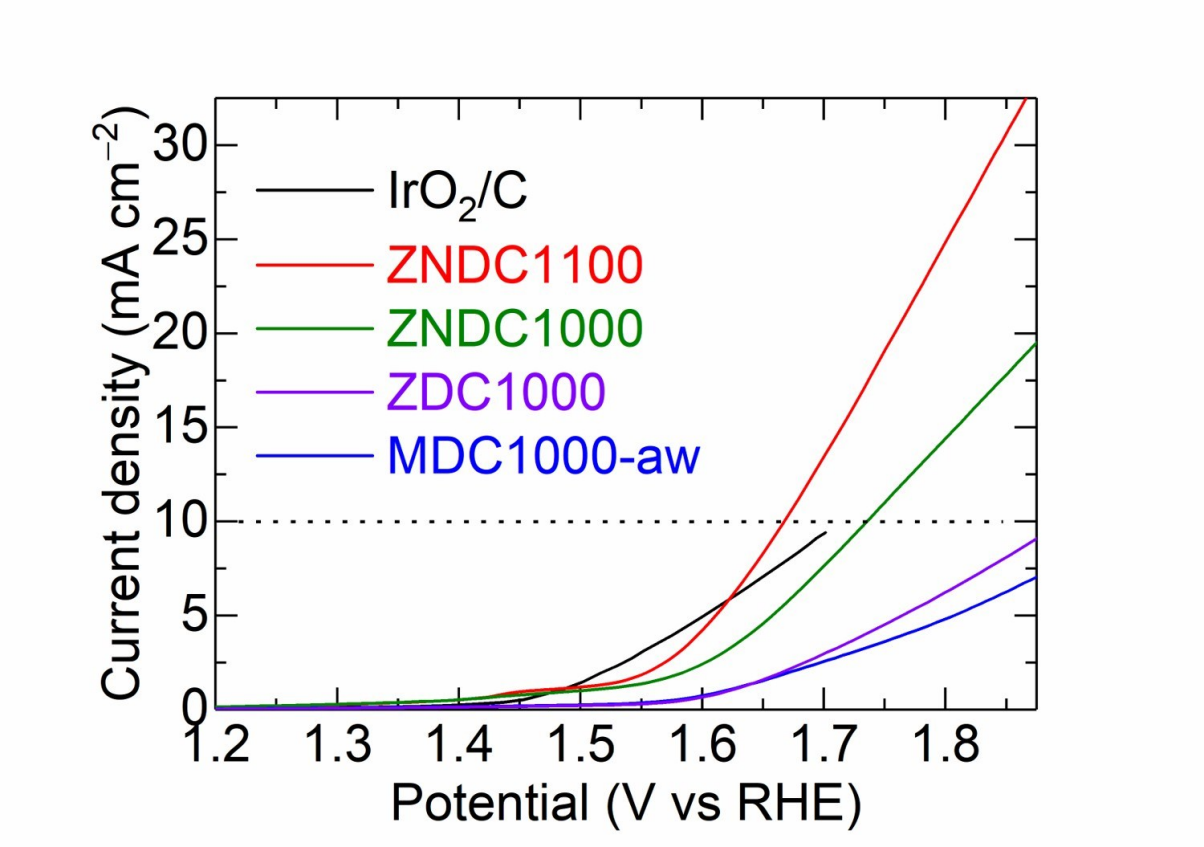

Figure S18. Comparative OER activity curves of the samples show a significantly enhanced catalytic activity in the hybrid ZNDC samples over the simple nitrogen doped porous ZDC1000 sample or dopant free MDC1000-aw sample. A benchmark reference sample, IrO_2/C [ref. 32] is also included to show our sample, ZNDC1100 superior activity.

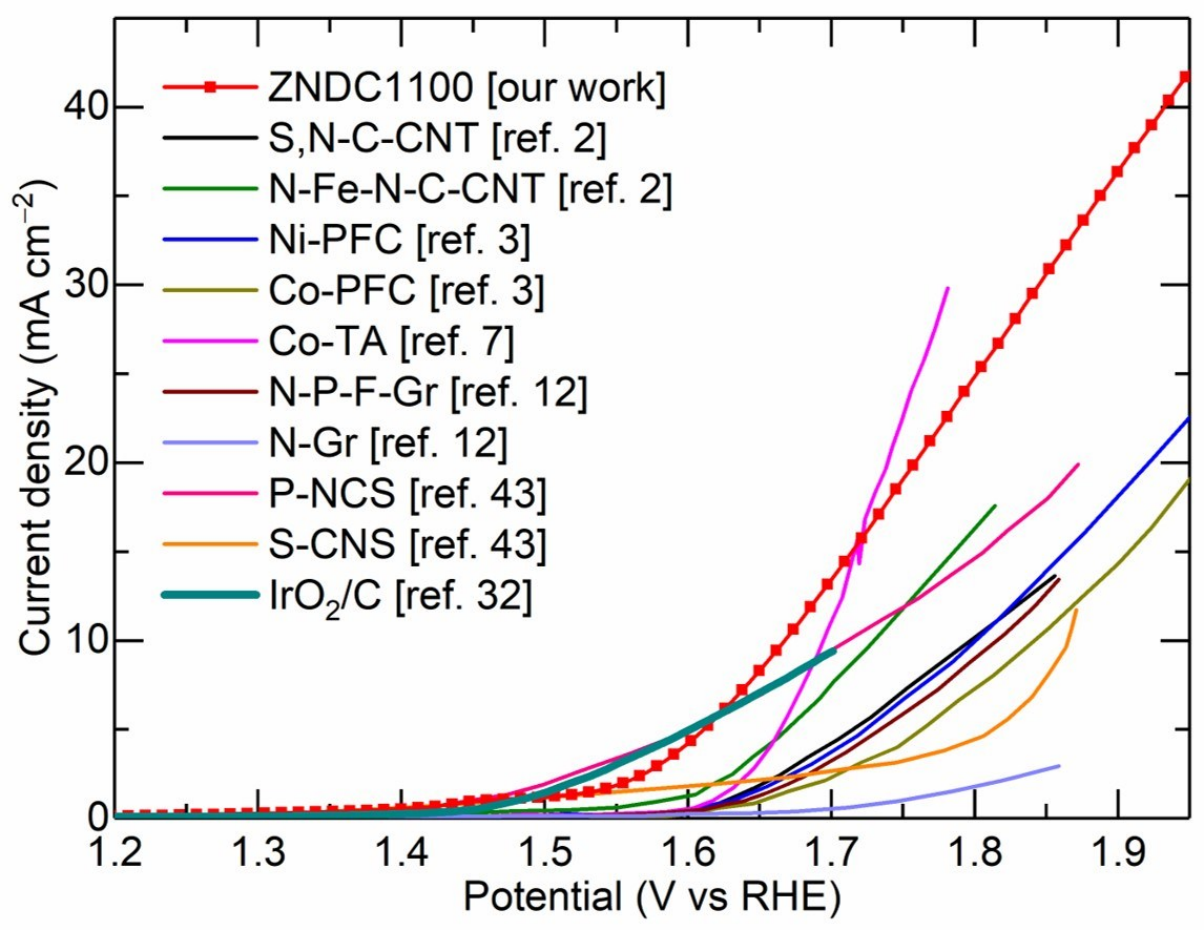

Figure S19. Comparative OER data curves of our ZNDC1100 with the literature samples of metal/alloy-doped (N-, S, P-)-carbon structures, include graphene-, nanotube- and porous carbon- based network substrates. Reference IrO_2/C sample is also included as a standard. All the data were recorded in a 0.1 M KOH electrolyte at 1600 rpm of the rotating disk electrode (see the references in the main paper for full details).

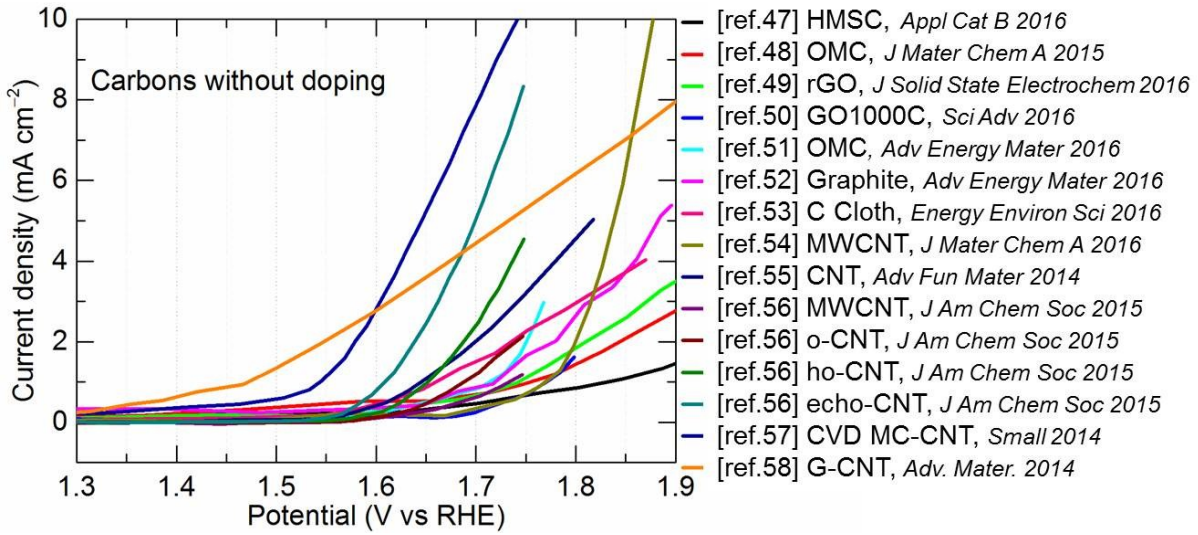

Figure S20. Comparative OER data curves of the literature samples of pristine/ or oxidized carbon structures, include graphene (G or reduced graphene oxide, rGO)-, nanotube (CNT, or MWCNT)- and porous carbon (HMSC-hollow mesoporous shell carbon, OMC-ordered mesoporous carbon, C cloth-carbon cloth)- based network substrates. All the data were recorded in a 0.1 M KOH electrolyte (see the list of additional references for full details).

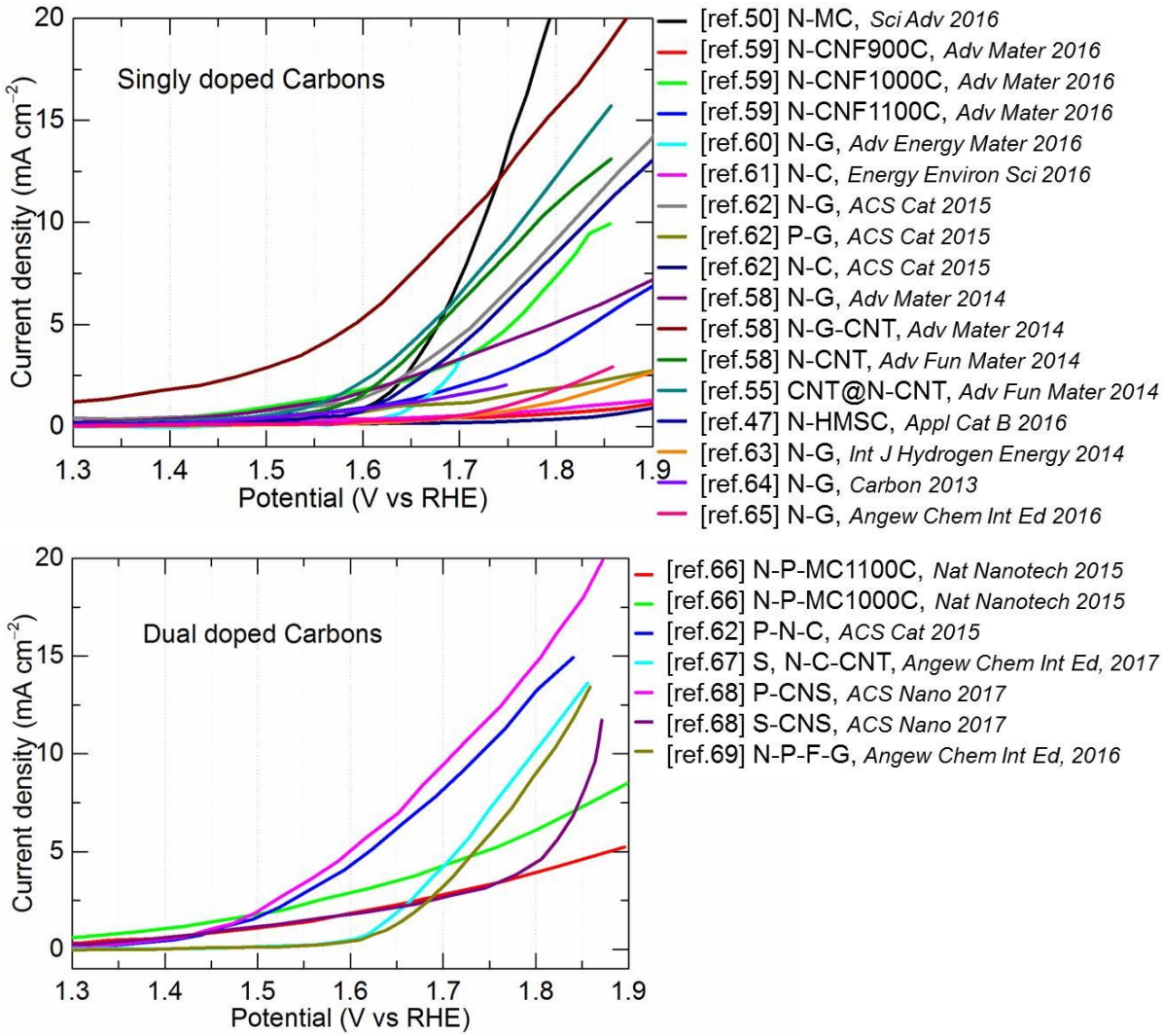

Figure S21. Comparative OER data curves of the literature samples of metal-free, N-, P-, S-doped carbon structures, include graphene (G)-, nanotube/nanofiber (CNT/CNF)- and porous carbon (HMSC-hollow mesoporous shell carbon, MC-mesoporous carbon, C-porous carbon, CNS-carbon nitride sponge)- based network substrates. All the data were recorded in a 0.1 M KOH electrolyte (see the list of additional references for full details).

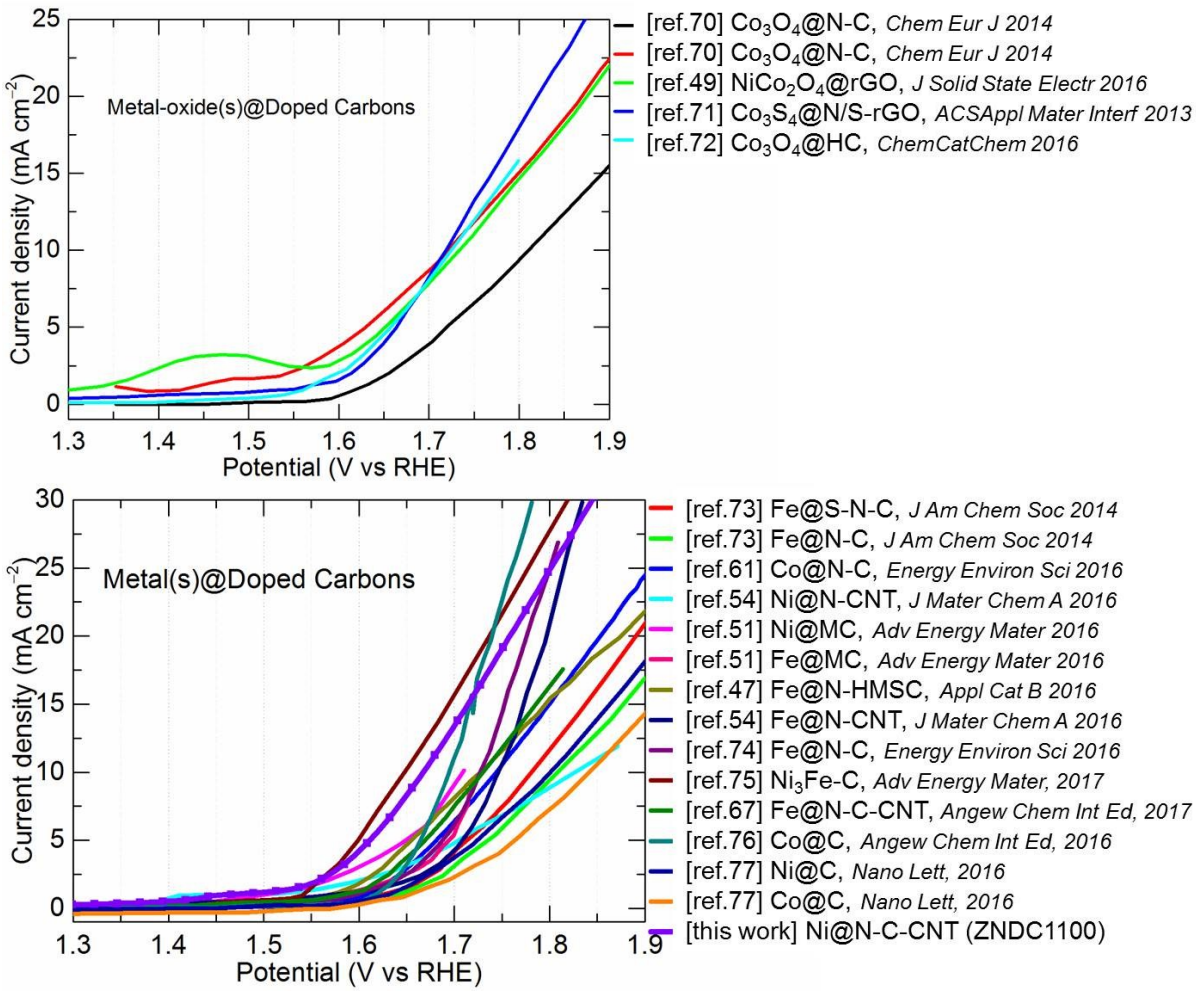

Figure S22. Comparative OER data curves of the literature samples of metal / alloy / metal-oxides @ doped carbon structures, include graphene (rGO, or G)-, nanotube (CNT, or MWCNT)- and porous carbon (HMSC-hollow mesoporous shell carbon, MC-mesoporous carbon, C-porous carbon)- based network substrates. All the data were recorded in a 0.1 M KOH electrolyte. (see the list of additional references for full details).

Additional References

47. M. Y. Song, D.-S. Yang, K. P. Singh, J. Yuan, J.-S. Yu, Nitrogen-doped hollow carbon spheres with highly graphitizedmesoporous shell: role of Fe for oxygen evolution reaction, *Appl. Catal. B: Environ*., 2016, **191,** 202.
48. P. Li, R. Ma, Y. Zhou, Y. Chen, Z. Zhou, G. Liu, Q. Liu, G. Peng, Z. Liang, J. Wang, In situ growth of spinel $CoFe_2O_4$ nanoparticles on rod-like ordered mesoporous carbon for bifunctional electrocatalysis of both oxygen reduction and oxygen evolution, *J. Mater. Chem. A*, **2015**, *3*, 15598.

49. E. Umeshbabu, G. Rajeshkhanna, P. Justin, G. R. Rao, $NiCo_2O_4$/rGO hybrid nanostructures for efficient electrocatalytic oxygen evolution, *J. Solid State Electrochem*, **2016**, *20*, 2725.
50. H. B. Yang, J. Miao, S.-F. Hung, J. Chen, H. B. Tao, X. Wang, L. Zhang, R. Chen, J. Gao, H. M. Chen, L. Dai, B. Liu, Identification of catalytic sites for oxygen reduction and oxygen evolution in N-doped graphene materials: development of highly efficient metal-free bifunctional electrocatalyst, *Sci. Adv*., **2016**, *2*, e1501122.
51. J. Y. Cheon, K. Kim, Y. J. Sa, S. H. Sahgong, Y. Hong, J. Woo, S.-D. Yim, H. Y. Jeong, Y. Kim, S. H. Joo, Graphitic nanoshell/mesoporous carbon nanohybrids as highly efficient and stable bifunctional oxygen electrocatalysts for rechargeable aqueous Na-air batteries, *Adv. Energy Mater*., **2016**, *6*, 1501794.
52. X. Yu, M. Zhang, J. Chen, Y. Li, G. Shi, Nitrogen and sulfur codoped graphite foam as a self-supported metal-free electrocatalytic electrode for water oxidation, *Adv. Energy Mater*., **2016**, *6*, 1501492.
53. J. Lai, S. Li, F. Wu, M. Saqib, R. Luque, G. Xu, Unprecedented metal-free 3D porous carbonaceous electrodes for full water splitting, *Energy Environ. Sci*., **2016**, *9*, 1210.
54. Y. Liu, H. Jiang, Y. Zhu, X. Yang, C. Li, Transition metals (Fe, Co, and Ni) encapsulated in nitrogen-doped carbon nanotubes as bi-functional catalysts for oxygen electrode reactions, *J. Mater. Chem. A*, **2016**, *4*, 1694.
55. G.-L. Tian, Q. Zhang, B. Zhang, Y.-G. Jin, J.-Q. Huang, D. S. Su, F. Wei, Toward full exposure of "active sites": nanocarbon electrocatalyst with surface enriched nitrogen for superior oxygen reduction and evolution reactivity, *Adv. Funct. Mater*., **2014**, *24*, 5956.
56. X. Lu, W.-L. Yim, B. H. R. Suryanto, C. Zhao, Electrocatalytic oxygen evolution at surface-oxidized multiwall carbon nanotubes, *J. Am. Chem. Soc*., **2015**, *137*, 2901.
57. G.-L. Tian, M.-Q. Zhao, D. Yu, X.-Y. Kong, J.-Q. Huang, Q. Zhang, F. Wei, Nitrogen-doped graphene/carbon nanotube hybrids: in situ formation on bifunctional catalysts and their superior electrocatalytic activity for oxygen evolution/reduction reaction, *Small*, **2014**, *10*, 2251.
58. S. Chen, J. Duan, M. Jaroniec, S.-Z. Qiao, Nitrogen and oxygen dual-doped carbon hydrogel film as a substrate-free electrode for highly efficient oxygen evolution reaction, *Adv. Mater*., **2014**, *26*, 2925.
59. Q. Liu, Y. Wang, L. Dai, J. Yao, Scalable fabrication of nanoporous carbon fiber films as bifunctional catalytic electrodes for flexible Zn-air batteries, *Adv. Mater*., **2016**, *28*, 3000.
60. J. Masa, P. Weide, D. Peeters, I. Sinev, W. Xia, Z. Sun, C. Somsen, M. Muhler, W. Schuhmann, Amorphous Cobalt Boride (Co_2B) as a Highly Efficient Nonprecious Catalyst for Electrochemical Water Splitting: Oxygen and Hydrogen Evolution, *Adv. Energy Mater*. **2016,** *6*, 1502313.
61. S. Gadipelli, T. Zhao, S. A. Shevlin, Z. Guo, Switching effective oxygen reduction and evolution performance by controlled graphitization of a cobalt–nitrogen–carbon framework system, *Energy Environ. Sci*., **2016**, *9*, 1661.
62. R. Li, Z. Wei, X. Gou, Nitrogen and phosphorus dual-doped graphene/carbon nanosheets as bifunctional electrocatalysts for oxygen reduction and evolution, *ACS Catal*., **2015**, *5*, 4133.
63. L. Wang, F. Yin, C. Yao, N-doped graphene as a bifunctional electrocatalyst for oxygen reduction and oxygen evolution reactions in an alkaline electrolyte, *Int. J. Hydrogen Energy*, **2014**, *39*, 15913.
64. Z. Lin, G. H. Waller, Y. Liu, M. Liu, C. Wong, Simple preparation of nanoporous few-layer nitrogen-doped graphene for use as an efficient electrocatalyst for oxygen reduction and oxygen evolution reactions, *Carbon*, **2013**, *53*, 130.

65. J. Zhang, L.Dai, Nitrogen, phosphorus, and fluorine tri-doped graphene as a multifunctional catalyst for self-powered electrochemical water splitting, *Angew. Chem. Int. Ed*., **2016**, *55*, 13296.
66. J. Zhang, Z. Zhao, Z. Xia, L. Dai, A metal-free bifunctional electrocatalyst for oxygen reduction and oxygen evolution reactions, *Nat. Nanotech.,* **2015,** *10,* 444.
67. P. Chen, T. Zhou, L. Xing, K. Xu, Y. Tong, H. Xie, L. Zhang, W. Yan, W. Chu, C. Wu, Y. Xie, Atomically dispersed iron–nitrogen species as electrocatalysts for bifunctional oxygen evolution and reduction reactions, *Angew. Chem. Int. Ed.* **2017**, *56*, 610.
68. S. S. Shinde, C.-H. Lee, A.Sami, D.-H. Kim, S.-U. Lee, J.-H. Lee, Scalable 3-D carbon nitride sponge as an efficient metal-free bifunctional oxygen electrocatalyst for rechargeable Zn-air batteries, *ACS Nano*, **2017**, *11*, 347.
69. J. Zhang, L. Dai, Nitrogen, phosphorus, and fluorine tri-doped graphene as a multifunctional catalyst for self-powered electrochemical water splitting, *Angew. Chem. Int. Ed*. **2016**, *55*, 13296.
70. W. Chaikittisilp, N. L. Torad, C. Li, M. Imura, N. Suzuki, S. Ishihara, K. Ariga, Y. Yamauchi, Synthesis of nanoporous carbon-cobalt-oxide hybrid electrocatalysts by thermal conversion of metal-organic frameworks, *Chem. Eur. J.,* **2014**, *20*, 4217.
71. Q. Liu, J. Jin, J. Zhang, $NiCo_2S_4$@graphene as a bifunctional electrocatalyst for oxygen reduction and evolution reactions, *ACS Appl. Mater. Interfaces*, **2013**, *5*, 5002.
72. J. Wang, Z. Wu, L. Han, R. Lin, H. L. Xin, D. Wang, Hollow-structured carbon-supported nickel cobaltite nanoparticles as an efficient bifunctional electrocatalyst for the oxygen reduction and evolution reactions, *ChemCatChem*, **2016**, *8*, 736.
73. N. R. Sahraie, J. P. Paraknowitsch, C. Göbel, A. Thomas, P. Strasser, Noble-metal-free electrocatalysts with enhanced ORR performance by task-specific functionalization of carbon using ionic liquid precursor systems, *J. Am. Chem. Soc*., **2014**, *136*, 14486.
74. S. Dresp, F. Luo, R. Schmack, S. Kuhl, M. Gliech, P. Strasser, An efficient bifunctional two-component catalyst for oxygen reduction and oxygen evolution in reversible fuel cells, electrolyzers and rechargeable air electrodes, *Energy Environ. Sci*., **2016**, *9*, 2020.
75. G. Fu, Z. Cui, Y. Chen, Y. Li, Y. Tang, J. B. Goodenough, Ni_3Fe-N doped carbon sheets as a bifunctional electrocatalyst for air cathodes, *Adv Energy Mater*, **2017**, *7*, 160117.
76. J. Wei, Y. Liang, Y. Hu, B. Kong, J. Zhang, Q. Gu, Y. Tong, X. Wang, S. P. Jiang, H. Wang, Hydrothermal synthesis of metal-polyphenol coordination crystals and their derived metal/N-doped carbon composites for oxygen electrocatalysis, *Angew. Chem. Int. Ed.,* **2016**, *55*, 12470.
77. G. Fu, Y. Chen, Z. Cui, Y. Li, W. Zhou, S. Xin, Y. Tang, J. B. Goodenough, Novel hydrogel-derived bifunctional oxygen electrocatalyst for rechargeable air cathodes, *Nano Lett*., **2016**, *16*, 6516.